basal of the two. Such a placement of the more terrestrially adapted *Ichthyostega* (*16*), taken together with the features indicating weight-bearing ability (ventrally facing radial and ulnar facets) of the very primitive ANSP 21350 (*9*), would suggest a scenario of rapid early terrestrialization rather different from the currently predominant "aquatic Devonian tetrapods" model.

### References and Notes


1. H. Blom, *Palaeontology* **48**, 111 (2005).
2. E. Jarvik, *Fossils Strata* **40**, 1 (1996).
3. M. I. Coates, *Trans. R. Soc. Edinburgh Earth Sci.* **87**, 363 (1996).
4. See supporting material on *Science* Online.
5. S. M. Andrews, T. S. Westoll, *Trans. R. Soc. Edinburgh* **68**, 207 (1970).
6. E. I. Vorobyeva, *Paleontol. J.* **34**, 632 (2000).
7. C. A. Boisvert, E. Mark-Kurik, P. E. Ahlberg, *Nature* **456**, 636 (2008).
8. N. H. Shubin, E. B. Daeschler, F. A. Jenkins, *Nature* **440**, 764 (2006).
9. N. H. Shubin, E. B. Daeschler, M. I. Coates, *Science* **304**, 90 (2004).
10. O. A. Lebedev, M. I. Coates, *Zool. J. Linn. Soc.* **114**, 307 (1995).
11. J. A. Clack, S. M. Finney, *J. Syst. Palaeontol.* **2**, 311 (2005).
12. S. J. Godfrey, *Philos. Trans. R. Soc. London Ser. B* **323**, 75 (1989).
13. R. Holmes, *Philos. Trans. R. Soc. London Ser. B* **306**, 431 (1984).
14. M. Ruta, M. I. Coates, D. L. J. Quicke, *Biol. Rev. Cambridge Philos. Soc.* **78**, 251 (2003).
15. P. E. Ahlberg, J. A. Clack, E. Luksevics, H. Blom, I. Zupins, *Nature* **453**, 1199 (2008).
16. P. E. Ahlberg, J. A. Clack, H. Blom, *Nature* **437**, 137 (2005).



17. We thank the Geological Museum, Copenhagen, for the loan of specimens; the staff of the University of Texas CT unit for scanning MGUH f.n. 301a; N. Shubin for access to the *Tiktaalik* material; and E. Rayfield for help with the Amira modeling software. Supported by a Churchill Fellowship from the Winston Churchill Foundation (V.C.) and by Vetenskapsrådet (the Swedish Research Council) (P.E.A.).


### Supporting Online Material

www.sciencemag.org/cgi/content/full/324/5925/364/DC1
Materials and Methods
SOM Text
Figs. S1 to S4
Table S1
Movie S1
References


22 October 2008; accepted 5 March 2009
10.1126/science.1167542


# A Ferroelectric Oxide Made Directly on Silicon


**Maitri P. Warusawithana,[1] Cheng Cen,[2] Charles R. Sleasman,[2] Joseph C. Woicik,[3] Yulan Li,[4] Lena Fitting Kourkoutis,[5] Jeffrey A. Klug,[6] Hao Li,[7] Philip Ryan,[8] Li-Peng Wang,[9,10] Michael Bedzyk,[6,11] David A. Muller,[5] Long-Qing Chen,[4] Jeremy Levy,[2] Darrell G. Schlom[1]***



Metal oxide semiconductor field-effect transistors, formed using silicon dioxide and silicon, have undergone four decades of staggering technological advancement. With fundamental limits to this technology close at hand, alternatives to silicon dioxide are being pursued to enable new functionality and device architectures. We achieved ferroelectric functionality in intimate contact with silicon by growing coherently strained strontium titanate ($SrTiO_3$) films via oxide molecular beam epitaxy in direct contact with silicon, with no interfacial silicon dioxide. We observed ferroelectricity in these ultrathin $SrTiO_3$ layers by means of piezoresponse force microscopy. Stable ferroelectric nanodomains created in $SrTiO_3$ were observed at temperatures as high as 400 kelvin.


For decades, semiconductor device designers have envisioned numerous devices using ferroelectrics in combination with semiconductors. These concepts include nonvolatile memories (*1*, *2*), "smart" transistors that can be used as temperature or pressure sensors (*3*), and ferroelectric field-effect transistors whose logic states require no power to maintain (*4*, *5*). Missing, however, has been the ability to integrate ferroelectrics directly with mainstream semiconductors. Our work bridges this gap, demonstrating ferroelectric functionality in a $SrTiO_3$ thin film grown directly, without any intermediate layers and free of reaction, on the workhorse of semiconductor technology, silicon.

Recent work has explored ways to use epitaxial strain to induce or enhance ferroelectricity in thin films (*6*–*8*). Ferroelectric responses that are distinct from naturally occurring bulk ferroelectrics have also been obtained through the growth of nano-engineered superlattices containing different dielectric and ferroelectric phases (*9*–*11*). In all of the above-referenced studies, the substrate and film are isostructural. For commensurate $SrTiO_3$/(001) Si, the interface is structurally far more complex, connecting a diamond structure (silicon) with a perovskite ($SrTiO_3$) (Fig. 1). The high reactivity of silicon with many elements and their oxides (*12*) presents a formidable challenge to the integration of functional oxides with silicon, as does the tendency of a pristine silicon surface to rapidly form its own oxide.

Using molecular beam epitaxy (MBE), we have deposited epitaxial $SrTiO_3$ films on (001) Si substrates via a kinetically controlled growth process (*13*, *14*) (fig. S1), which synchrotron diffraction measurements reveal to be commensurately strained up to a thickness of ~24 Å. The growth method used differs substantially from those reported previously (*15*–*17*) for the epitaxial integration of $SrTiO_3$ with silicon (*13*) (figs. S1 and S2). Although bulk $SrTiO_3$ is not ferroelectric at any temperature, the large compressive strain (~1.7%) induced on commensurately strained $SrTiO_3$/Si is predicted to result in ferroelectricity (*13*, *18*) with a Curie temperature ($T_C$) near room temperature (fig. S3 and table S1) and an out-of-plane polarization (*6*, *8*, *19*). Films whose thickness exceeds the equilibrium critical thickness (*20*), however, are unstable to relaxation, which would lower the transition temperature and produce nanoscale heterogeneity.

We discuss data from five $SrTiO_3$ films identified by their nominal thickness in molecular layers (ML): 5 ML, 6 ML, 8 ML, 10 ML, and 20 ML. These $SrTiO_3$ films were grown on (001) Si substrates by MBE, in layers of one to a few molecular strata at a time, until the desired thickness was reached (*13*). The silicon substrates used in this study were doped with n-type phosphorus ($1 \times 10^{15}$ to $5 \times 10^{15}$ phosphorus atoms/cm$^3$) having a resistivity of 1 to 4 ohm·cm. Each layer that was grown involved a controlled sequence of

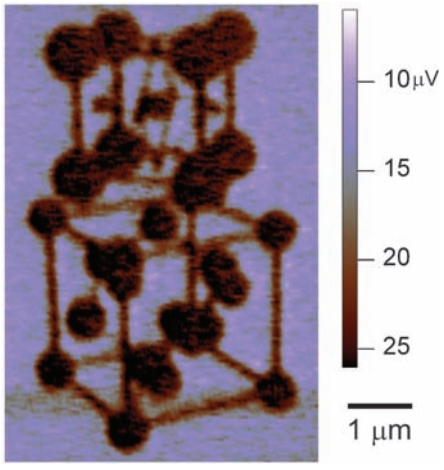


**Fig. 1.** Structure of the $SrTiO_3$/Si interface, written and imaged on a 6 ML $SrTiO_3$/Si sample by PFM. With the 45° in-plane rotational offset between the unit cells (*15*), the epitaxial orientation relationship is (001) $SrTiO_3$ // (001) Si and [110] $SrTiO_3$ // [100] Si.


[1]Department of Materials Science and Engineering, Cornell University, Ithaca, NY 14853, USA. [2]Department of Physics and Astronomy, University of Pittsburgh, Pittsburgh, PA 15260, USA. [3]National Institute of Standards and Technology, Gaithersburg, MD 20899, USA. [4]Department of Materials Science and Engineering, Pennsylvania State University, University Park, PA 16802, USA. [5]School of Applied and Engineering Physics, Cornell University, Ithaca, NY 14853, USA. [6]Department of Physics and Astronomy, Northwestern University, Evanston, IL 60208, USA. [7]Applied Research and Technology Center, Motorola Inc., Tempe, AZ 85284, USA. [8]Ames Laboratory, Ames, IA 50011, USA. [9]Intel Corporation, Santa Clara, CA 95052, USA. [10]TricornTech, San Jose, CA 95129, USA. [11]Department of Materials Science and Engineering, Northwestern University, Evanston, IL 60208, USA.

*To whom correspondence should be addressed. E-mail: schlom@cornell.edu

steps (*13*, *14*) that kinetically suppress the oxidation of the substrate and reduce the tendency of the film to form islands (*21*) (fig. S4).

X-ray diffraction reveals the structural quality and strain relaxation that occurs in the $SrTiO_3$ films as thickness is increased. Rocking curves in ω [where the angle of incidence (θ) between the x-ray beam and the sample is rocked while leaving the detector position (2θ) fixed] of the out-of-plane $SrTiO_3$ 002 reflection are shown in Fig. 2A. Each curve displays an intense and narrow central peak due to coherently strained $SrTiO_3$ on top of a broad background peak (*13*). The height of the sharp central peak in relation to the background on this log intensity scale gives an indication of the fraction of the $SrTiO_3$ film that is coherently strained. The coherently strained fraction of the $SrTiO_3$ films decreases as the film thickness is increased. The full width at half maximum (FWHM) of the 5 ML sample, 0.012°, is representative of the sharpness of the coherent peaks (fig. S5).

We used x-ray diffraction to determine the in-plane strain of the $SrTiO_3$ films (*13*, *22*). Because the out-of-plane lattice constant of $SrTiO_3$ is distinct from that of silicon, the in-plane lattice constant of $SrTiO_3$ can be obtained by measuring an off-axis $SrTiO_3$ reflection where there is no overlap with a substrate peak. Figure 2C shows scans made through the $SrTiO_3$ 202 peak for the 5 ML, 6 ML, 8 ML, and 20 ML samples. The sharp peak observed at $h = k = 2.00$ Si reciprocal lattice units (r.l.u.) is due to the commensurate portion of the $SrTiO_3$ films with in-plane lattice constant = $a_{Si}/\sqrt{2} = 3.840$ Å. As the film thickness increases, the relative integrated intensity of the sharp peak decreases while that of a broad peak at $h = k < 2.00$ Si r.l.u. increases. The plot clearly shows the transition from mostly commensurate $SrTiO_3$ to mostly relaxed $SrTiO_3$ as the film thickness is increased. Reciprocal space maps of the $SrTiO_3$ 202 peak for the 6 ML and 8 ML samples are shown in Fig. 2, B and D, respectively. The 6 ML sample (Fig. 2B) has its diffracted intensity mostly centered at $h = k =$ 2.00 Si r.l.u., whereas for the 8 ML sample (Fig. 2D), more spectral weight is observed at lower values of $h = k$ (i.e., at larger in-plane lattice constants) because of relaxation of the $SrTiO_3$. The reciprocal space map for the 8 ML sample also shows how the spectral weight tails off to higher $\ell$ with smaller $h = k$ as strain relaxation sets in. From $\ell$ scans made across the coherent peak at $h = k = 2.00$ Si r.l.u., we find that the coherent peak occurs at $\ell \sim 2.71$ Si r.l.u.

To check for ferroelectricity in these strained $SrTiO_3$/(001) Si films, we used piezoresponse force microscopy (PFM), a technique that has been demonstrated on ferroelectric films as thin as 28 Å (*23*–*26*). With strain relaxation occurring for $SrTiO_3$/(001) Si film thickness as small as 8 ML (~32 Å), measurement of the piezoelectric

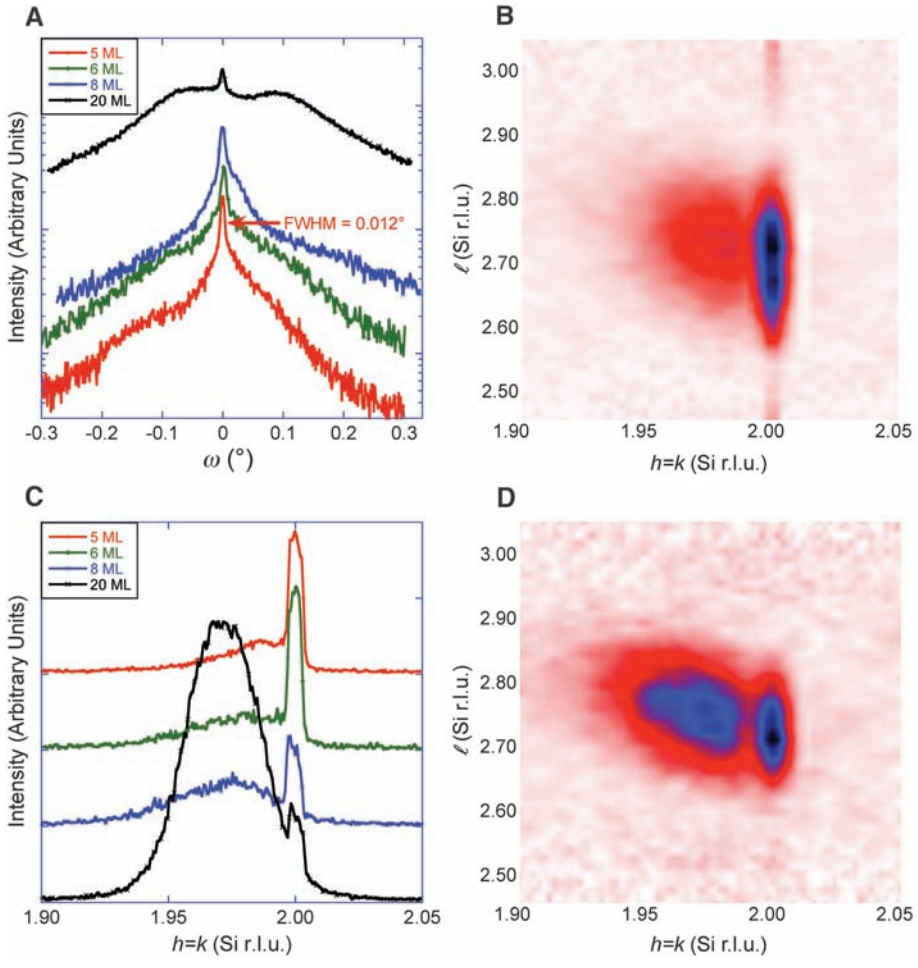


**Fig. 2.** The strain state of the $SrTiO_3$ films revealed by x-ray diffraction. (**A**) Rocking curves in ω of the out-of-plane $SrTiO_3$ 002 reflection. (**B**) Reciprocal space map of the 202 $SrTiO_3$ peak for the 6 ML sample. Note the beating along the $\ell$ direction. (**C**) Off-axis scans through the 202 $SrTiO_3$ peak. (**D**) Reciprocal space map of the 202 $SrTiO_3$ peak for the 8 ML sample. In (B) and (D), the intensity increases from white to red to blue to black.

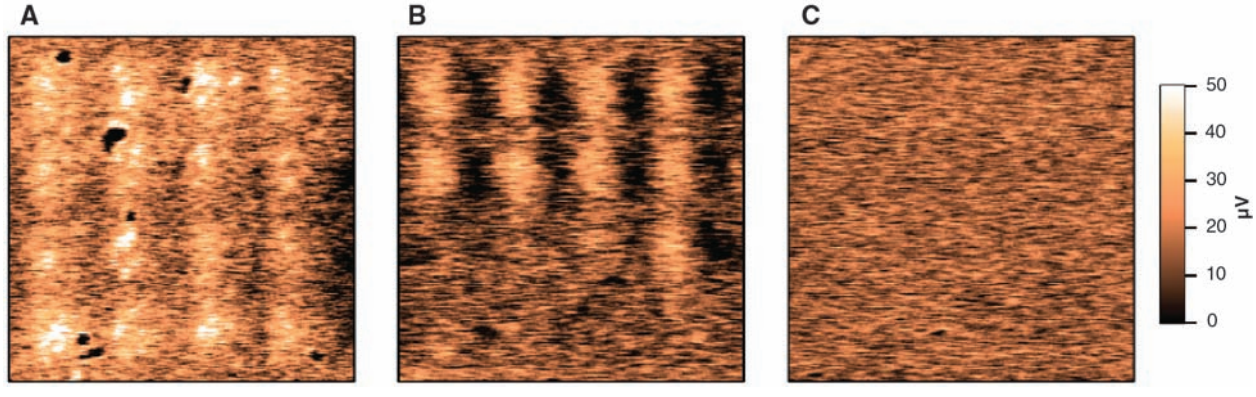


**Fig. 3.** PFM images (1 μm by 1 μm) of a 4 × 4 pattern of domains written on the 5 ML $SrTiO_3$/Si sample at different temperatures. (**A**) $T = 298$ K. (**B**) $T = 314$ K. (**C**) $T = 323$ K.

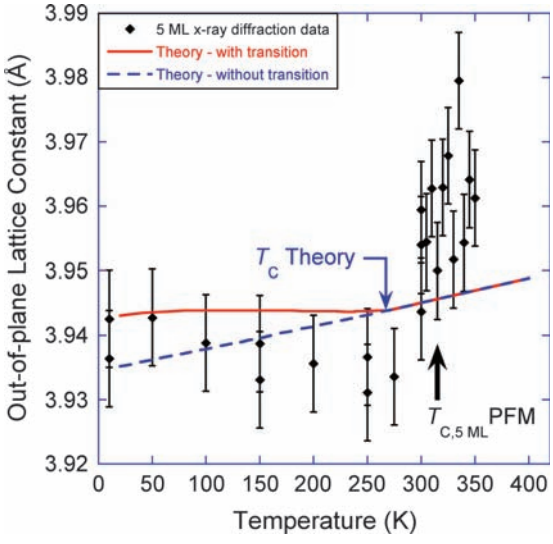


**Fig. 4.** Temperature dependence of the out-of-plane lattice constant of $SrTiO_3$ strained commensurately to the underlying silicon substrate. Theoretical prediction from thermodynamic analysis is shown, along with experimental data obtained from x-ray diffraction measurements of the 5 ML sample. The error bars reflect the maximum error expected considering systematic errors and variation in sample thickness. Some hysteresis between data taken on heating and cooling is evident. Also indicated is the transition temperature observed from PFM measurements for the 5 ML sample ($T_{C,5\ ML}$ PFM).

response of such thin layers is challenging. The large $d_{33}$ coefficients predicted for strained $SrTiO_3$/(001) Si (fig. S6), however, make it a reasonable signal to probe. Local electric fields were applied across the $SrTiO_3$ layer by means of a biased, conducting atomic force probe, and the resulting piezoelectric response of the strained $SrTiO_3$ film was subsequently imaged using the same probe (*13*). At room temperature, we found that domains of both polarities could be patterned on the 5 ML, 6 ML, 8 ML, and 10 ML samples, but not on the 20 ML sample. Figure 1 shows a PFM image written on the 6 ML sample at room temperature. In all of the samples that exhibited ferroelectricity via piezoresponse, a preferred downward polarization was observed (fig. S7). This agrees with reported x-ray fine structure measurements (*27*) and indicates that strained $SrTiO_3$ films on (001) Si are prepoled in their as-grown state. The lack of observable ferroelectricity in the 20 ML sample is consistent with x-ray diffraction measurements showing that the 20 ML sample is mainly relaxed (Fig. 2C) and helps rule out other possible mechanisms, such as changes in surface chemistry, for the observed piezoelectric response in other samples. A retention study of the written domains was also carried out for the 6 ML sample at room temperature (*13*) (figs. S8 and S9). The domain pattern was observed to be stable over a 72-hour period, at which point the pattern was erased by rastering the atomic-force probe with a constant voltage over the patterned area.

PFM measurements performed as a function of temperature revealed a rather sharp phase transition, above which ferroelectric domains are unstable. Figure 3 shows a series of three PFM measurements made on the 5 ML sample at different temperatures. Each image was acquired ~30 min after writing a 4 × 4 array of square domains. Although some features that are associated with imperfections on the sample surface also showed up on these images, at $T$ = 298 K each of the 16 domains could be observed (Fig. 3A). The temperature was increased, and at $T$ = 314 K only 9 of the 16 domains could be seen (Fig. 3B). The existence of a single domain on the third row from the top rules out a variety of possible measurement artifacts, such as a "wandering" cantilever resonance frequency. At $T$ = 323 K (Fig. 3C) or at higher temperatures, no stable domains could be observed. These PFM measurements provide a lower bound on the paraelectric-to-ferroelectric transition temperature ($T_C$): $T_{C,5\ ML} > 314$ K.

Measurements performed on the 6 ML sample, however, show that ferroelectric domains written on it are stable at even higher temperatures: $T_{C,6\ ML} > 410$ K (fig. S10). Such temperatures are much higher than that predicted by thermodynamic analysis (fig. S3). The theoretical calculation assumes an infinitely thick $SrTiO_3$ slab with complete polarization charge screening and with a uniform biaxial compressive strain equivalent to that obtained by growing commensurately strained $SrTiO_3$ on (001) Si. By leaving out surface effects such as structural and electronic discontinuities and the possibility of incomplete screening of the polarization charge, the thermodynamic analysis does not take into account the finite film thickness, which presumably would lead to a substantially reduced transition temperature, as has been shown for the related ferroelectrics $PbTiO_3$ (*28*) and $BaTiO_3$ (*29*). Thus, the observed experimental results indicate a substantially higher transition temperature than that predicted by theory. In the case of a metal in contact with a ferroelectric (*30*, *31*), polarization screening at the interface has been shown to enhance the ferroelectric $T_C$. Screening of the polarization charge as well as structural and electronic discontinuities at this heteroepitaxial $SrTiO_3$/Si interface, not considered in the present thermodynamic analysis, could play a role in understanding the quantitative differences between experiment and theory.

As an independent check of the ferroelectric phase transition, temperature-dependent x-ray diffraction measurements of the out-of-plane lattice constant were performed on the 5 ML sample (Fig. 4) to sense the structural transition (*7*, *8*, *32*) that should coincide with $T_C$. The average out-of-plane lattice constant was extracted from scans made of the $SrTiO_3$ 002 peak. With the in-plane lattice constant clamped to the silicon substrate and changing only by the thermal expansion of silicon, which is much smaller than that of $SrTiO_3$, the out-of-plane lattice constant should continuously expand with temperature in the absence of a structural transition. The measured out-of-plane lattice constant with temperature for the 5 ML sample shows a clear deviation from what is expected for thermal expansion with the in-plane lattice constant constrained to that of silicon. This deviation coincides in temperature with the transition temperature observed by PFM. The "kink" feature observed in the out-of-plane lattice constant with temperature (*7*, *8*, *32*) is qualitatively consistent with thermodynamic analysis of commensurate $SrTiO_3$/Si undergoing a ferroelectric transition (Fig. 4), although the agreement with $T_C$ is likely to be coincidental.

A ferroelectric in direct contact with silicon invites hybrid ferroelectric-semiconductor devices (*1*–*5*). Although the low or almost nonexistent conduction band offset predicted (*33*) and measured (*34*) between $SrTiO_3$ and silicon could lead to practical difficulties in implementing such ferroelectric devices, it has been proposed that this problem can be overcome by carefully constructing the interface between $SrTiO_3$ and silicon (*35*, *36*).

### References and Notes


1. M. Suzuki, *J. Ceram. Soc. Jpn. Int. Ed.* **103**, 1088 (1995).
2. P. Vettiger, G. Binnig, *Sci. Am.* **288**, 47 (January 2003).
3. Y.-R. Wu, J. Singh, *IEEE Trans. Electron. Dev.* **52**, 284 (2005).
4. J. A. Morton, U.S. Patent 2,791,761 (7 May 1957).
5. L. L. Chang, L. Esaki, *IBM Tech. Discl. Bull.* **14**, 1250 (1971).
6. J. H. Haeni *et al.*, *Nature* **430**, 758 (2004).
7. K. J. Choi *et al.*, *Science* **306**, 1005 (2004).
8. D. G. Schlom *et al.*, *Annu. Rev. Mater. Res.* **37**, 589 (2007).
9. M. P. Warusawithana, E. V. Colla, J. N. Eckstein, M. B. Weissman, *Phys. Rev. Lett.* **90**, 036802 (2003).
10. D. A. Tenne *et al.*, *Science* **313**, 1614 (2006).
11. E. Bousquet *et al.*, *Nature* **452**, 732 (2008).
12. K. J. Hubbard, D. G. Schlom, *J. Mater. Res.* **11**, 2757 (1996).
13. See supporting material on *Science* Online.
14. H. Li *et al.*, *J. Appl. Phys.* **93**, 4521 (2003).
15. H. Mori, H. Ishiwara, *Jpn. J. Appl. Phys.* **30**, L1415 (1991).
16. R. A. McKee, F. J. Walker, M. F. Chisholm, *Phys. Rev. Lett.* **81**, 3014 (1998).
17. Z. Yu *et al.*, *J. Vac. Sci. Technol. B* **18**, 2139 (2000).
18. A. Antons, J. B. Neaton, K. M. Rabe, D. Vanderbilt, *Phys. Rev. B* **71**, 024102 (2005).
19. N. A. Pertsev, A. K. Tagantsev, N. Setter, *Phys. Rev. B* **61**, R825 (2000).
20. J. W. Matthews, A. E. Blakeslee, *J. Cryst. Growth* **27**, 118 (1974).
21. L. F. Kourkoutis *et al.*, *Phys. Rev. Lett.* **100**, 036101 (2008).
22. J. C. Woicik *et al.*, *Phys. Rev. B* **73**, 024112 (2006).
23. C. H. Ahn *et al.*, *Science* **276**, 1100 (1997).
24. T. Tybell, C. H. Ahn, J. M. Triscone, *Appl. Phys. Lett.* **72**, 1454 (1998).
25. T. Tybell, C. H. Ahn, J. M. Triscone, *Appl. Phys. Lett.* **75**, 856 (1999).

26. C. Lichtensteiger *et al.*, *Appl. Phys. Lett.* **90**, 052907 (2007).
27. J. C. Woicik *et al.*, *Phys. Rev. B* **75**, 140103(R) (2007).
28. D. D. Fong *et al.*, *Science* **304**, 1650 (2004).
29. J. Junquera, P. Ghosez, *Nature* **422**, 506 (2003).
30. P. Ghosez, K. M. Rabe, *Appl. Phys. Lett.* **76**, 2767 (2000).
31. M. Stengel, D. Vanderbilt, N. A. Spaldin, http://arxiv.org/abs/0811.0632 (2008).
32. E. D. Specht, H.-M. Christen, D. P. Norton, L. A. Boatner, *Phys. Rev. Lett.* **80**, 4317 (1998).
33. J. Robertson, C. W. Chen, *Appl. Phys. Lett.* **74**, 1168 (1999).
34. S. A. Chambers, Y. Liang, Z. Yu, R. Droopad, J. Ramdani, *J. Vac. Sci. Technol. A* **19**, 934 (2001).
35. J. Junquera, M. Zimmer, P. Ordejón, P. Ghosez, *Phys. Rev. B* **67**, 155327 (2003).
36. C. J. Först, C. R. Ashman, K. Schwarz, P. E. Blöchl, *Nature* **427**, 53 (2004).



37. We thank C. H. Ahn, O. Auciello, V. Gopalan, D. A. Tenne, and F. J. Walker for stimulating discussions and interactions during the course of this work. Supported by Office of Naval Research grant N00014-04-1-0426 (M.P.W., L.F.K., D.A.M., and D.G.S.), NSF grants DMR-0507146 and DMR-0704022, Materials Research Science and Engineering Center program grants DMR-0520404, DMR-0520513, and DMR-0820404, and, for the work performed at Argonne National Laboratory, the U.S. Department of Energy, Basic Energy Sciences, Materials Sciences. Diffraction data were taken at sector 33BM of the Advanced Photon Source, which is supported by the U.S. Department of Energy, Basic Energy Sciences, Office of Science under contract W-31-109-ENG-38.


**Supporting Online Material**

www.sciencemag.org/cgi/content/full/324/5925/367/DC1
Materials and Methods
SOM Text
References
Figs. S1 to S10
Table S1


11 December 2008; accepted 26 February 2009
10.1126/science.1169678


# Anomalous Fractionations of Sulfur Isotopes During Thermochemical Sulfate Reduction


**Yumiko Watanabe,[1]* James Farquhar,[2] Hiroshi Ohmoto[1]**



Anomalously fractionated sulfur isotopes in many sedimentary rocks older than 2.4 billion years have been widely believed to be the products of ultraviolet photolysis of volcanic sulfur dioxide in an anoxic atmosphere. Our laboratory experiments have revealed that reduced-sulfur species produced by reactions between powders of amino acids and sulfate at 150° to 200°C possess anomalously fractionated sulfur isotopes: $\Delta^{33}S = +0.1$ to $+2.1$ per mil and $\Delta^{36}S = -1.1$ to $+1.1$ per mil. These results suggest that reactions between organic matter in sediments and sulfate-rich hydrothermal solutions may have produced anomalous sulfur isotope signatures in some sedimentary rocks. If so, the sulfur isotope record of sedimentary rocks may be linked to the biological and thermal evolution of Earth in ways different than previously thought.


Large anomalous fractionations of sulfur isotopes (*1*–*5*) are present in many sedimentary rocks older than 2.4 billion years and are virtually absent in younger rocks (*6*–*10*). It has been argued that sulfur-bearing minerals [such as pyrite ($FeS_2$) and barite ($BaSO_4$)] in sedimentary rocks older than 2.4 billion years formed from native sulfur ($S^0$) and/or sulfate ($SO_4^{2-}$: $S^{6+}$) produced by ultraviolet (UV) photolysis of volcanic sulfur dioxide ($SO_2$) in an $O_2$-poor atmosphere (*6*, *8*, *10*), and thus that the record of anomalously fractionated S isotopes is evidence for the transition from an anoxic to oxic atmosphere about 2.4 billion years ago (*7*, *11*). These arguments have been based on the assumption that the only processes producing anomalously fractionated S isotopes for both $\Delta^{33}S$ and $\Delta^{36}S$ (*2*, *6*) are photochemical reactions involving gaseous S-bearing species [such as hydrogen sulfide ($H_2S$) and $SO_2$] (*6*, *12*). Laboratory experiments performed with UV photolysis of $SO_2$ under an $O_2$-free condition produced $S^0$ and $SO_4^{2-}$ with large anomalous fractionations of S isotopes (*13*). A theoretical study also suggests a maximum partial pressure of oxygen ($PO_2$) of ~$10^{-6}$ atm in order for the UV photolysis of $SO_2$ to produce $S^0$ and $SO_4^{2-}$ (*14*). Here, we present experiments showing that reactions between powders of amino acids and $SO_4^{2-}$ can also produce anomalous fractionations of S isotopes.

$FeS_2$, the most abundant sulfide mineral in sedimentary rocks, forms from a variety of reactions involving $H_2S$ and Fe in sediments and solutions (*15*). Both bacterial sulfate reduction (BSR) and thermochemical sulfate reduction (TSR) using $SO_4^{2-}$ and organic matter in waters and sediments are important in the production of $H_2S$

$$2(C - C^*) + SO_4^{2-} + 2H^+ \rightarrow 2CO_2 + 2C^* + H_2S \quad (1)$$

where C and C* refer, respectively, to reactive and nonreactive (residual) carbon atoms in organic compounds. This reaction typically results in positive correlations between the $FeS_2$ and C* contents of sedimentary rocks (*15*). The C/C* ratio and reaction rate vary depending on the type and maturation degree of organic compounds (for example, carbohydrates, hydrocarbons, amino acids, bitumen, and type I, II, and III kerogens). BSR is carried out by sulfate-reducing bacteria (SRB),

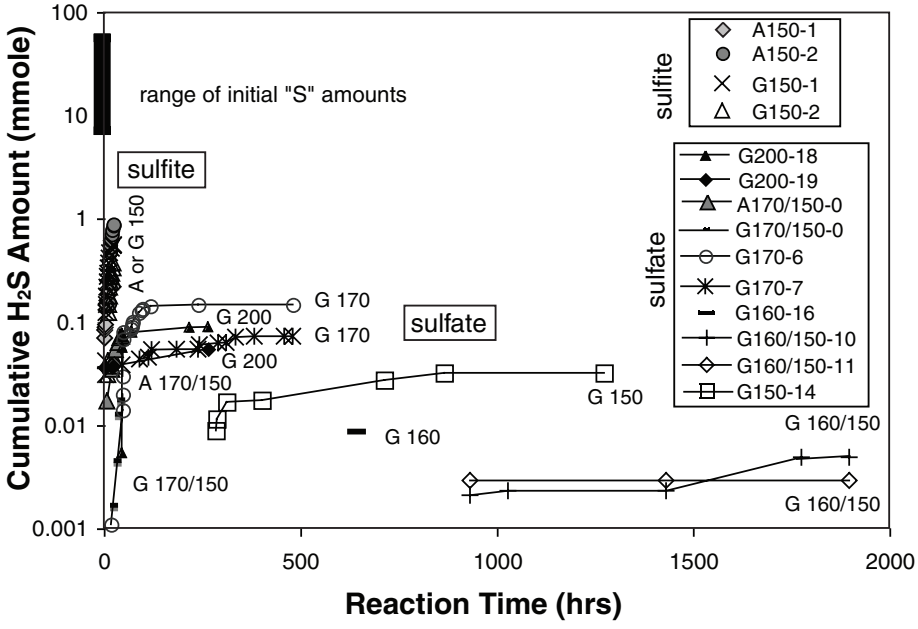


**Fig. 1.** Cumulative amounts of $H_2S$ produced from $SO_3^{2-}$ or $SO_4^{2-}$ reductions by amino acids (alanine or glycine). Gray symbols represent the experiments using alanine (A) and solid, open, cross, or bar symbols represent those using glycine (G). The three-digit numbers (150, 160, 170, and 200) represent experiment temperatures, and the hyphenated numbers represent the run numbers.


[1]The NASA Astrobiology Institute and Department of Geosciences, Pennsylvania State University, University Park, PA 16802, USA. [2]Department of Geology and Earth System Science Interdisciplinary Center, University of Maryland, College Park, MD 20742, USA.

*To whom correspondence should be addressed. E-mail: yumiko@geosc.psu.edu

# Supporting Online Material for

## A Ferroelectric Oxide Made Directly on Silicon

Maitri P. Warusawithana, Cheng Cen, Charles R. Sleasman, Joseph C. Woicik, Yulan Li, Lena Fitting Kourkoutis, Jeffrey A. Klug, Hao Li, Philip Ryan, Li-Peng Wang, Michael Bedzyk, David A. Muller, Long-Qing Chen, Jeremy Levy, Darrell G. Schlom*

*To whom correspondence should be addressed. E-mail: schlom@cornell.edu

Published 17 April 2009, *Science* **324**, 367 (2009)
DOI: 10.1126/science.1169678

**This PDF file includes:**

## Methods

### Film growth

$SrTiO_3$ films were grown using elemental strontium and titanium sources and molecular oxygen for oxygenation. Throughout each growth the quality of the films was extensively monitored in situ using reflection high-energy electron diffraction (RHEED). The silicon substrates (3" diameter; *n*-type (phosphorous); resistivity = 1-4 Ω·cm; (001) oriented within ±0.1º) were cleaned using a commercial UV ozone cleaner for ~20 minutes before loading into the molecular beam epitaxy (MBE) chamber. The chamber pressure was below $2\times10^{-9}$ Torr at all times except for when oxygen was introduced. The substrate temperature ($T_{sub}$) was measured by an optical pyrometer at temperatures above 550 ºC and by a thermocouple (with an accuracy of ± 50 ºC) at lower temperatures. During each deposition step discussed below, the substrate was continuously rotated. The native surface oxide of the silicon substrate was thermally removed in situ prior to film growth via a strontium-assisted deoxidation process (*S1*) by depositing ~2 molecular layers (ML) of strontium metal after heating the substrate to 600 ºC. The $SiO_2$ layer desorbed, with strontium acting as a catalyst, when the substrate was heated to ~800 ºC. The oxide removal was observed by the transformation of the amorphous RHEED pattern to one showing characteristic features of a crystalline (001) Si surface (see Fig. S1A).

With this deoxidation scheme, a fractional molecular layer of strontium remains bonded to the silicon surface once the $SiO_2$ is removed. Its presence is manifested in RHEED as a superposition of a 2× and a 3× surface reconstruction along the [110] azimuth of (001) Si when the substrate is cooled to 600 ºC (see Fig. S1B). This superposition of surface reconstructions arises from a strontium coverage between 1/6 ML (in which case only a 3× reconstruction would be observed) and ½ ML (in which case only a 2× reconstruction would be observed) bonded at the silicon surface (*S2*,*S3*). More strontium was deposited at 600 ºC until a clear 2× pattern along the [110] azimuth of (001) Si was observed corresponding to a total of ½ ML of strontium at the surface.

Strontium and titanium sources were carefully adjusted during a calibration film grown just prior to the actual film such that the strontium and titanium fluxes were precisely matched at $\sim1\times10^{13}$ atoms/cm$^2$·s. This precise flux matching was achieved by

first using a quartz crystal microbalance to obtain starting values for strontium and titanium fluxes. Using these initial fluxes, the calibration sample was grown by codepositing strontium and titanium in an oxygen background pressure $\geq 2\times10^{-7}$ Torr and a substrate temperature of ~700 ºC. During this calibration film, using RHEED as a guide, the temperature of the strontium cell or the current through the Ti Ball (*S4*) was adjusted such that characteristic surface reconstructions due to excess strontium or excess titanium (see Fig. S2) did not appear for a long period of $SrTiO_3$ growth. This calibration process yielded a relative difference between strontium and titanium fluxes of less than 0.3%.

The oxygen flow was meticulously controlled using a piezoelectrically controlled leak valve to give a molecular oxygen flow of approximately $2\times10^{16}$ molecules/s injected at a 30º angle to the substrate from a 1 cm diameter tube that is placed ~22 cm from the substrate. If this flow were sustained, the chamber pressure would eventually reach a steady state background pressure of ~$1.5\times10^{-7}$ Torr.

With the substrate temperature at ~300 ºC, oxygen, strontium and titanium were codeposited to form 2.5 ML of $SrTiO_3$. During the growth (which lasted ~2.5 min.) the chamber background pressure typically increased into the upper $10^{-8}$ Torr range before the oxygen flow was stopped. In this as-grown state, the $SrTiO_3$ film is epitaxial, although the crystal quality was improved by heating up in vacuum (less than $2\times10^{-9}$ Torr) to ~580 ºC for ~10 min. (see Fig. S1C & Fig. S1D). To grow a thicker film, the sample was cooled down to ~330 ºC and a further 1 or 2 ML of $SrTiO_3$ was added followed by another vacuum anneal. This process was continued until the desired thickness was reached. The $SrTiO_3$ films grown in this manner showed a crystalline diffraction pattern in RHEED at each step of the sequenced growth (Fig. S1). X-ray diffraction measurements carried out on these $SrTiO_3$/Si films showed crystalline quality comparable to single crystal $SrTiO_3$ substrates (Fig. S5). By contrast, the growth process discussed in ref. S5 proceeds through recrystallization of an amorphous layer. The amorphous initiation of the growth in this latter process is believed to impede the chances of obtaining a commensurately strained $SrTiO_3$ film on (001) Si (*S6*). A third method of growing $SrTiO_3$/(001) Si (*S7*), which takes a high-temperature growth approach, was also found to result in films that were not commensurate with silicon showing an elastic

anomaly due to differential thermal expansion between $SrTiO_3$ and silicon (*S8*). Moreover, this growth scheme resulted in an extended $SiO_2$ layer at the $SrTiO_3$/Si interface (*S9*). Although optical Raman measurements have shown evidence for symmetry breaking in films grown by this high-temperature process (*S10,S11*), the signal observed was attributed to dislocations and local strain in the vicinity of defects in the crystal (*S10*) and therefore, cannot be attributed to a consequence of ferroelectricity (*S11*).

**Piezo-force Microscopy**

Scanning probe microscopy was used to observe ferroelectric domains. A commercial atomic force microscope (AFM) (Asylum MFP-3D) was employed using Pt-coated (OMCL-AC240TM-W2) or diamond-coated (CDT-FMR-10) silicon cantilevers. Piezo-force microscope (PFM) images were acquired using the following protocol: A voltage was applied to the tip: $V(t)=V_{tip}+V_{ac}\cos(\omega t)$, where $\omega$ is an angular frequency chosen to be close to the resonant frequency of the cantilever-sample system while in contact mode. The ac deflection of the cantilever was measured optically and detected using a lock-in amplifier. The phase of the lock-in amplifier was calibrated before each measurement such that a positive signal of the in-phase ($X$) channel was observed for sufficiently large $V_{tip}$ bias. All signals acquired were taken from the $X$ channel in this fashion. To read ferroelectric domains $V_{tip}$ was set to 0 V.

Ferroelectric writing was achieved using the following protocol: A voltage $V_{tip}(x,y)$ was specified that corresponds to the image one intends to write (e.g., atomic structure of $SrTiO_3$/Si interface or an array of squares). The tip was held fixed while the sample position was scanned in a raster fashion such that $(x(t),y(t))$ sweeps out the entire area to be written. A voltage $V_{tip}(x(t),y(t))$ was applied as the sample was rastered to produce the desired domain structure.

## Thermodynamic Analysis

Fig. S3 presents a phase stability diagram for $(001)_p$ oriented $SrTiO_3$ thin films as a function of the in-plane biaxial strain $e_0$, where the subscript *p* refers to the pseudocubic Miller index. The biaxial strain $e_0$ is the average in-plane strain along $[100]_p$ and $[010]_p$ axes of the $SrTiO_3$ film from its underlying substrate and $e_0>0$ means that the film is under tensile strain.

All the possible stable phases in the biaxially strained $(001)_p$ $SrTiO_3$ films shown in Fig. S3 are listed in Table S1. In the table, the letters, '**T**' and '**O**', indicate crystallographically 'tetragonal' and 'orthorhombic' symmetries, respectively. The superscripts, '*P*', '*S*' or '*F*', distinguish paraelectric, antiferrodistortive structural (or ferroelastic), and ferroelectric phases. The vectors, $\mathbf{p} = (p_1, p_2, p_3)$ and $\mathbf{q} = (q_1, q_2, q_3)$, are the spontaneous polarization and the linear oxygen displacement corresponding to simultaneous out-of-phase rotations of oxygen octahedra around one of their four-fold symmetry axes. They are the order parameters to describe the ferroelectric transition and the antiferrodistortive phase transition. Fig. S3 is obtained using thermodynamic analysis. The stable phase at a given temperature and constraint strain minimizes the total energy of the films. Additional details maybe found in ref. S12.

The piezoelectric coefficient $d_{33}$ (see Fig. S6) was also calculated using its definition of $d_{33} = \partial e_{33}/\partial E_3$, where $E_3$ is the applied electric field component on the $SrTiO_3$ film along the out-of-plane direction, $e_{33}$ is the strain of the film along the same direction and is related to the polarization $\mathbf{p} = (0,0, p_3)$ and the antiferrodistortive structural order parameter $\mathbf{q} = (0,0, q_3)$ of the tetragonal *c*-phase (phase $\mathbf{T}_1^F$ or $\mathbf{T}_2^F$ shown in Fig. S3) by $e_{33} = p_3^2(Q_{11} + 2c_{12}Q_{12}/c_{11}) + q_3^2(\Lambda_{11} + 2c_{12}\Lambda_{12}/c_{11}) - 2c_{12}e_0/c_{11}$, where $c_{ij}$, $Q_{ij}$ and $\Lambda_{ij}$ are the elastic stiffness, electrostrictive coefficients and the linear-quadratic coupling coefficients between the strain and the structural order parameter, respectively. $p_3$ and $q_3$ are obtained by taking the minimum of the total energy density of $f_{total} = f_{bulk}(p_3, q_3) + f_{elastic}^{f}(p_3, q_3, e_0) - E_3 p_3$. The bulk energy density $f_{bulk}$ and the elastic energy density of the film $f_{elastic}^{f}$ are given in ref. S12.

It is seen that the piezoelectric coefficient $d_{33}$ (Fig. S6) increases with increasing temperature. The sharp change around 240 K is associated with the disappearance of the AFD structural transition, i.e. $q_3$=0. $d_{33}$ reaches a maximum at the ferroelectric transition temperature.

## X-ray Diffraction Measurements

The rocking curves through the $SrTiO_3$ 002 reflection presented in Fig. 2A contain both a narrow central specular component and a broad diffuse scattering component. While the full width at half maximum of the specular component reflects the atomic order coherency length, the diffuse intensity describes longer-range correlated structure or in some cases periodic (coherent) order. For the 20 ML film, the rocking curve diffuse scattering satellite features relate to long-range lateral domain ordering within the ordered oxide film. It is postulated that this domain ordering forms due to the silicon substrate surface step morphology (*S13*) as the $SrTiO_3$ fully latches to the underlying Si (001) surface.

As the $SrTiO_3$ film grows 45º rotated with respect to the in-plane silicon lattice (*S14*), $SrTiO_3$[100]//Si[110], for a film completely clamped to the silicon substrate the position of the $SrTiO_3$ 200 peak occurs at the exact position of the Si 220 diffraction, making it hard to distinguish the film peak. Since the 110 reflection is forbidden for silicon, the $SrTiO_3$ 100 reflection should appear background-free, providing a means to extract the in-plane lattice constant of the $SrTiO_3$ film. In practice, the crystal truncation rods that connect the allowed 111 and $11\bar{1}$ silicon reflections pass through the Si 110 point in reciprocal space (or close to the Si 110 point if the substrate has a miscut), complicating the interpretation of the data at the $SrTiO_3$ 100 reflection. Therefore, to unambiguously determine the in-plane strain of the $SrTiO_3$ films, it is necessary to measure an off-axis $SrTiO_3$ reflection (*S15*) where there is no overlap with a substrate peak due to the distinct out-of-plane lattice constants of $SrTiO_3$ and silicon.

## Bistability of Ferroelectric Polarization

Fig. S7A shows a PFM image of a 4x4 array of square domains written on a pristine surface (not previously scanned) of a 5 ML thick $SrTiO_3$/Si sample using a tip voltage of $V_{tip}$ = 2 V with respect to the silicon substrate, which is grounded. A similar experiment performed using a negative bias $V_{tip}$ = –2 V (Fig. S7B) shows that the writing of stable domains with both polarities is possible on the same area. A line cut across both images reveals a net positive piezoresponse that is observed in the areas that were not poled in either direction (Fig. S7C & Fig. S7D). This positive background response indicates that the as-grown film is pre-poled downward (i.e., positive charge density at the $SrTiO_3$/Si interface). This result is consistent with *ab initio* calculations as well as x-ray fine structure measurements (*S16*).

## Retention Study

A pattern consisting of four squares was written with $V_{tip}$= –4 V on the 6 ML thick $SrTiO_3$/Si sample at room temperature with the background written at $V_{tip}$= +4 V. The pattern was imaged approximately 20 times at regular intervals. Fig. S8 shows some of the PFM images obtained during this 72-hour period. The image is essentially unchanged, except for a small lateral shift due to thermal drift of the AFM. We find the domain pattern to be stable over a 72-hour period. There is a reduction in contrast due to changes in the resonant frequency of the cantilever; the spatial resolution is also apparently decreased, again due to wearing of the AFM tip as can be seen from the topography images (Fig. S9) obtained simultaneously with the PFM images of Fig. S8A. Subsequent images on fresh areas showed a resolution comparable to that of the image at 71 hr. of Fig. S8A.

The domain pattern was subsequently erased by applying a constant $V_{tip}$= –4 V to the same area. The PFM image (Fig. S8B), taken simultaneously during the erase operation, shows a slight remnant of the original image. Its existence arises from the fact that the advancing line scan has only erased half of the image in the vicinity of the probe. Subsequent erase scans do not show any trace of the original domain pattern, nor do PFM images taken at zero bias ($V_{tip}$= 0 V, Fig. S8C).

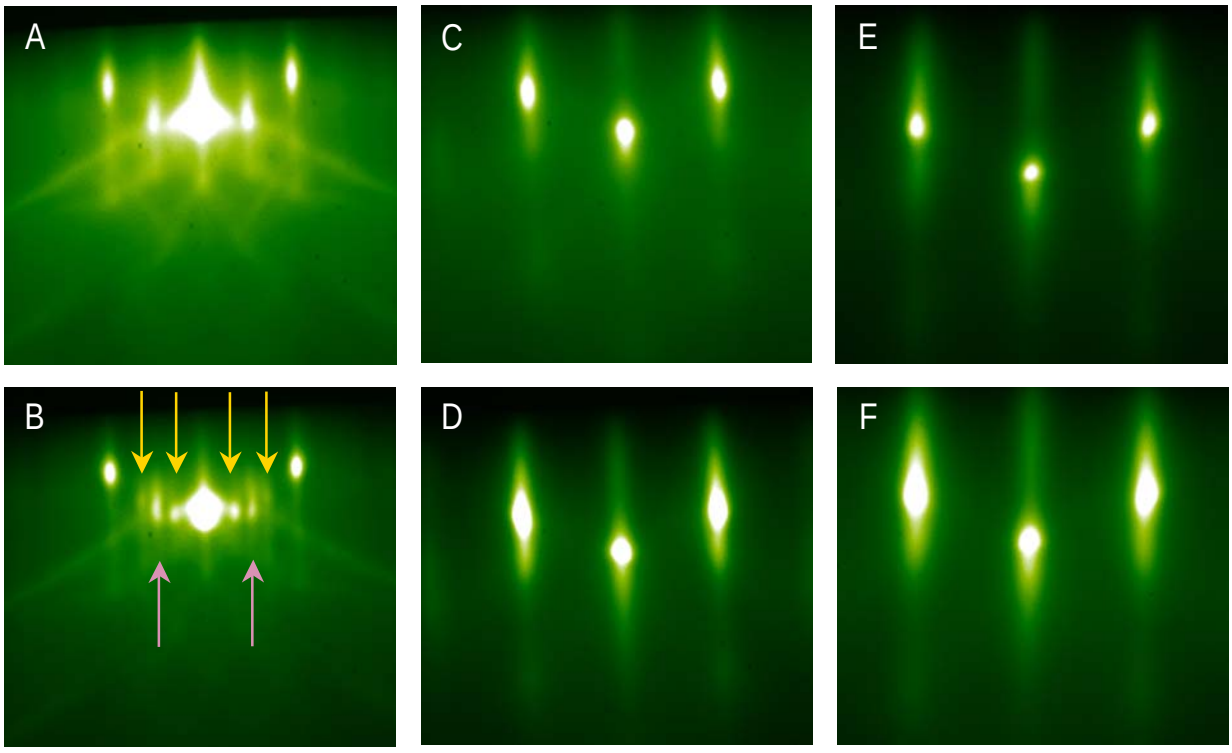


**Fig. S1.** RHEED images at different stages of the growth of $SrTiO_3$/(001) Si. (**A**) After strontium-assisted deoxidation at ~800 ºC along the [110] azimuth of (001) Si showing a 2× reconstruction. (**B**) Superposition of 2× and 3× surface reconstructions observed as the substrate is cooled to ~600 ºC. Pink and orange arrows indicate the streaks due to the 2× and 3× reconstructions, respectively. (**C**) At $T_{sub}$~300 ºC, the as-grown 2.5 ML thick $SrTiO_3$/Si film. (**D**) The 2.5 ML thick $SrTiO_3$/Si film surface after heating to $T_{sub}$~580 ºC. (**E**) The 5 ML thick $SrTiO_3$/Si film at $T_{sub}$~300 ºC. (**F**) Final surface of the 5 ML thick $SrTiO_3$/Si film after heating to $T_{sub}$~580 ºC.

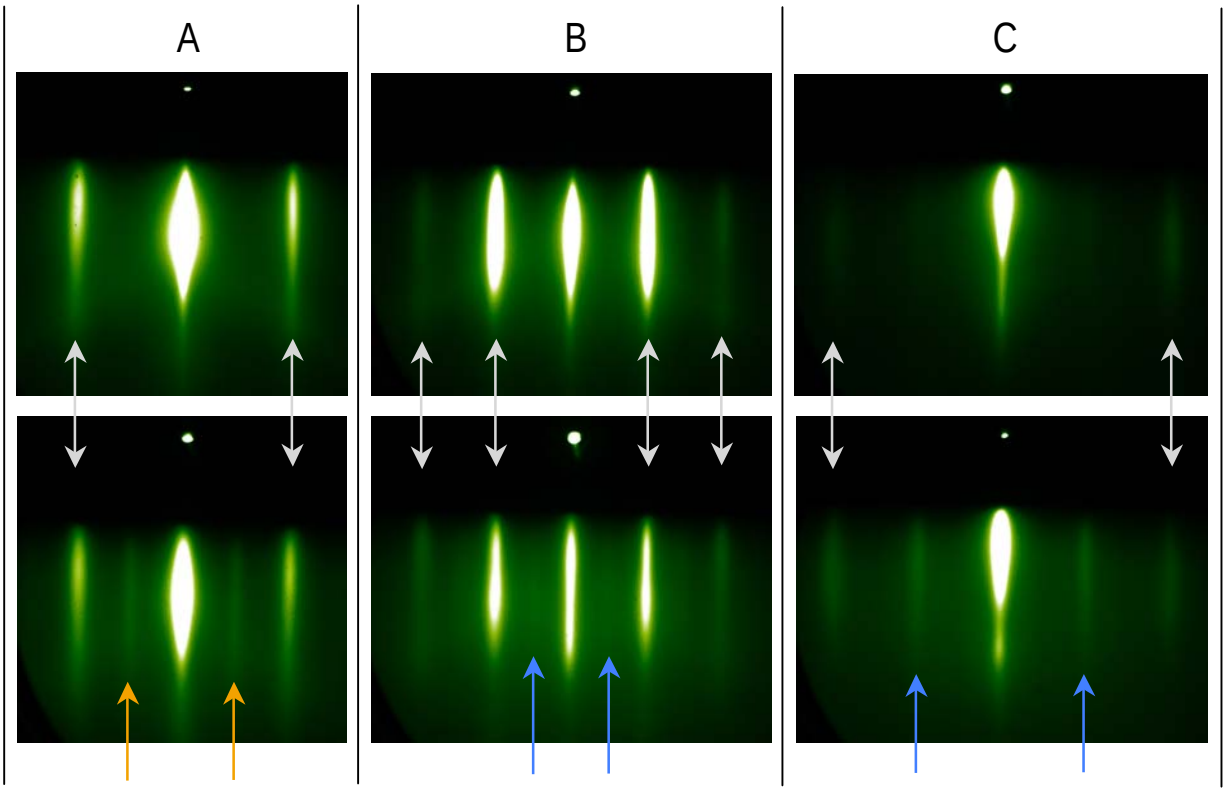


**Fig. S2.** RHEED patterns observed from a stoichiometric $SrTiO_3$ surface (top) and characteristic surface reconstructions observed that point to excess strontium or titanium during $SrTiO_3$ growth (bottom). (**A**) Along the [110] azimuth of $SrTiO_3$. Orange arrows indicate extra streaks that lead to a 2× reconstruction due to excess strontium. (**B**) Along the [100] azimuth and (**C**) along the [210] azimuth of $SrTiO_3$. Blue arrows indicate extra streaks that lead to 2× reconstructions due to excess titanium.

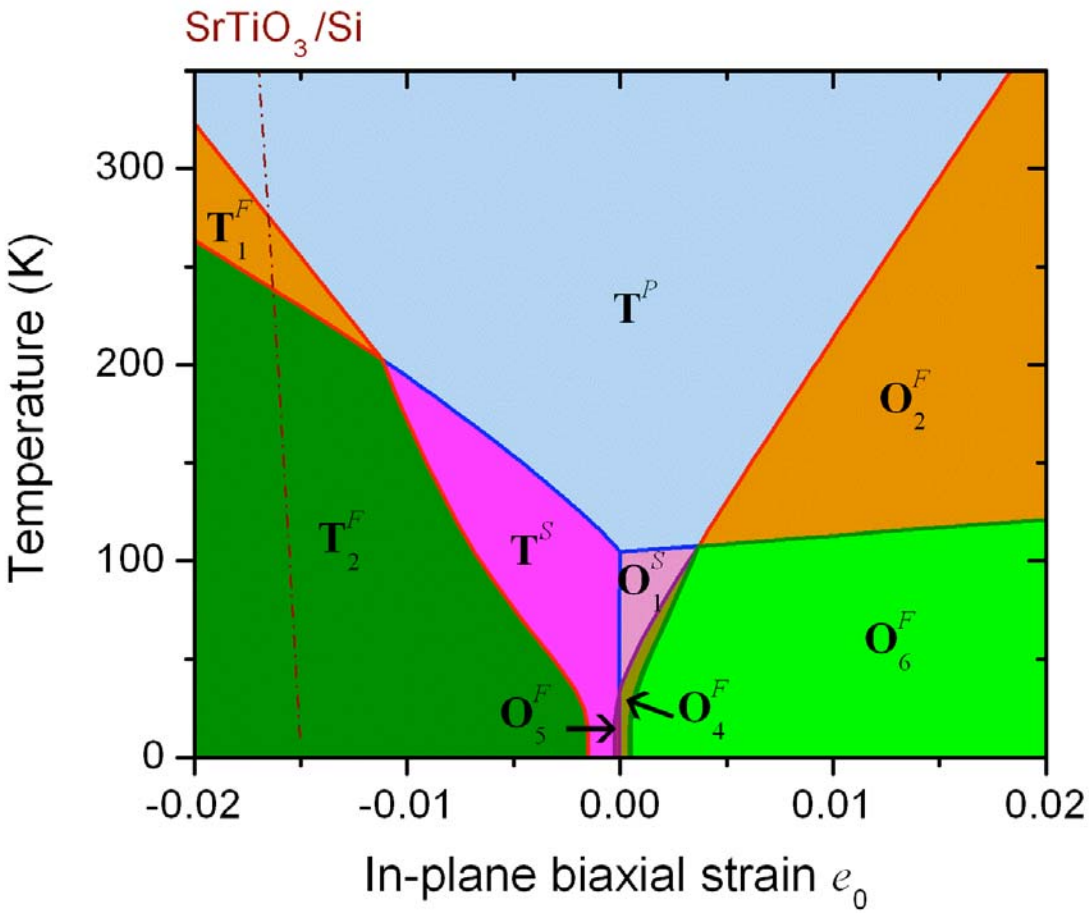


**Fig. S3.** Phase diagram for $SrTiO_3$ under varying amounts of biaxial strain. Commensurate growth on silicon corresponds to ~1.7% compressive strain at room temperature (indicated at left). The predicted phase transition is predicted to occur just below room temperature.

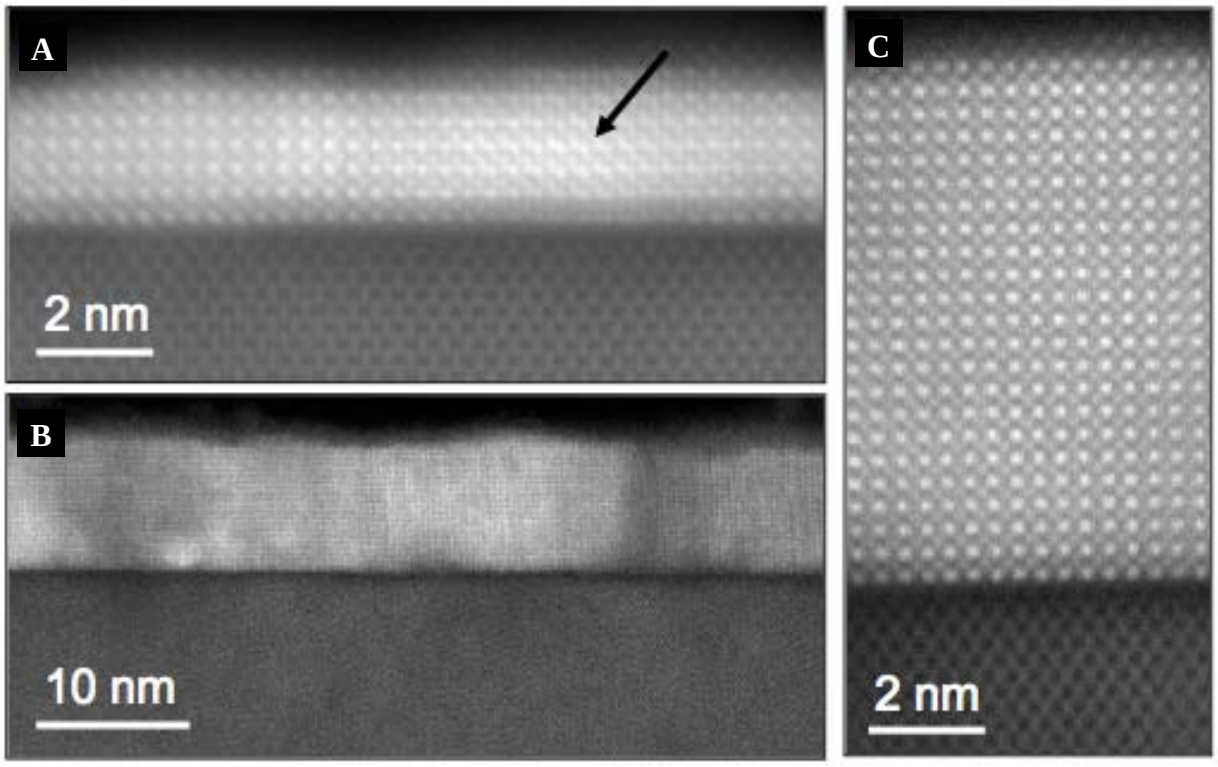


**Fig. S4.** Cross-sectional annular dark field (ADF) scanning transmission electron microscopy (STEM) images of $SrTiO_3$ films grown on (001) Si. (**A)** The image of the nominally 5 ML thick $SrTiO_3$ film shows an average film thickness of 6.5 unit cells suggesting a nonuniform $SrTiO_3$ coverage. In the area marked with an arrow more than one $SrTiO_3$ grain is imaged in projection. (**B**) Lower and (**C**) higher magnification images of the nominally 20 ML thick $SrTiO_3$ film confirming the absence of an extended interface layer. The ADF images were recorded on a 200 kV FEI Tecnai F20-ST STEM with a minimum probe size of 1.6 Å, a convergence semiangle of (9.5±0.5) mrad and an inner detector angle of 65 mrad. To increase signal to noise and average out the scan noise for the higher magnification images (**A**) and (**C**), 10 and 6 successive images, each recorded at 10 and 8 microseconds per pixel, were cross-correlated and averaged. Subsequently, the 1024×1024 pixel image was rebinned to 512×512 pixels.

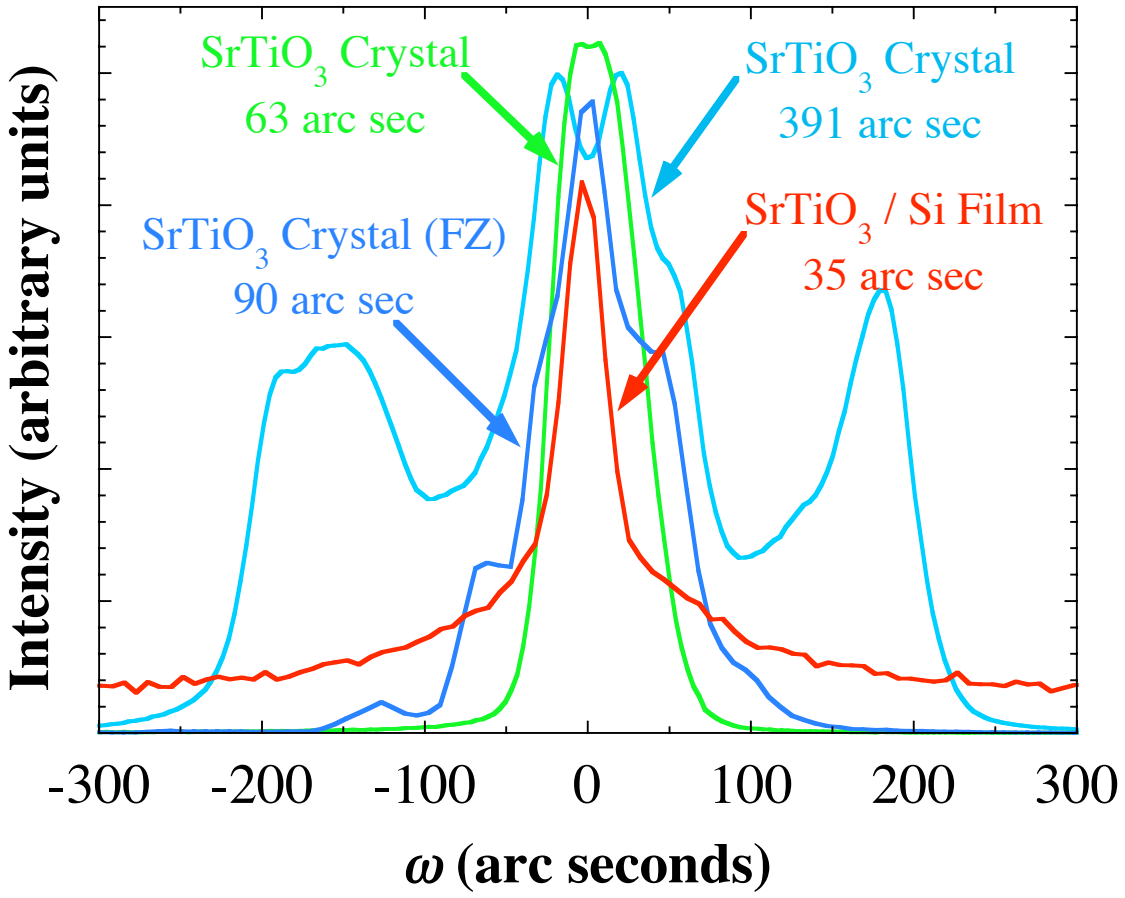


**Fig. S5.** X-ray diffraction rocking curves in $\omega$ of the out-of-plane $SrTiO_3$ 002 reflection of single crystal $SrTiO_3$ substrates and of the 10 ML thick $SrTiO_3$ film grown on (001) Si. The narrow rocking curve of the $SrTiO_3$/Si film indicates its excellent crystalline quality, comparable to single crystal $SrTiO_3$ substrates.

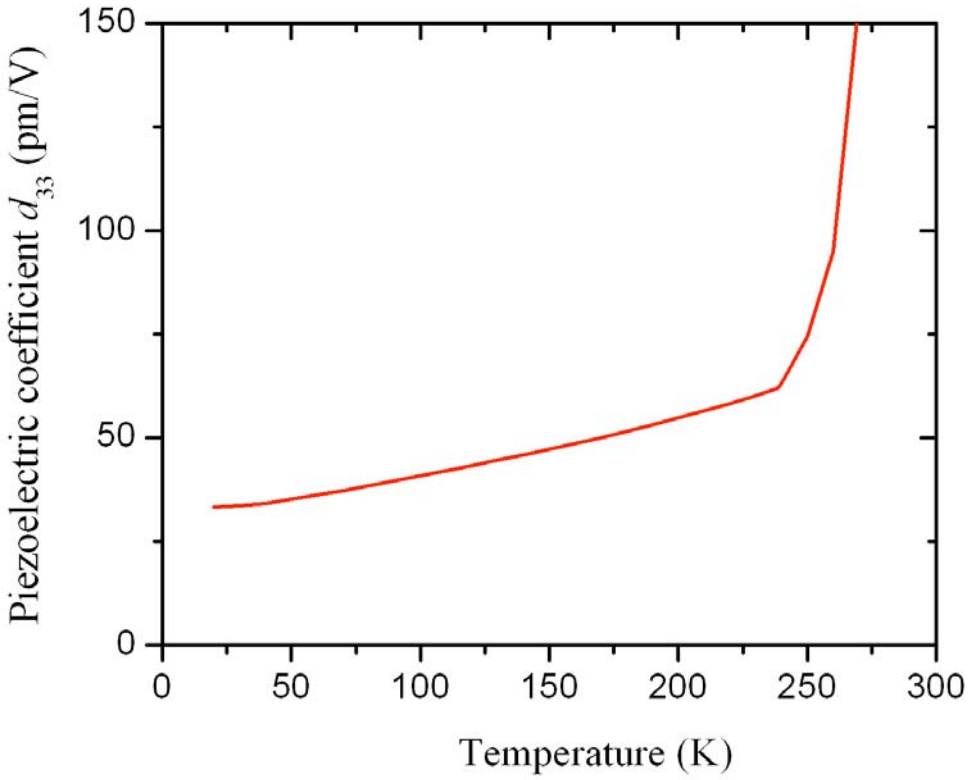


**Fig. S6.** Predicted piezoelectric coefficient $d_{33}$ as a function of temperature for commensurate $SrTiO_3$/(001) Si. See section on *Thermodynamic Analysis* for details of the calculation leading to this prediction.

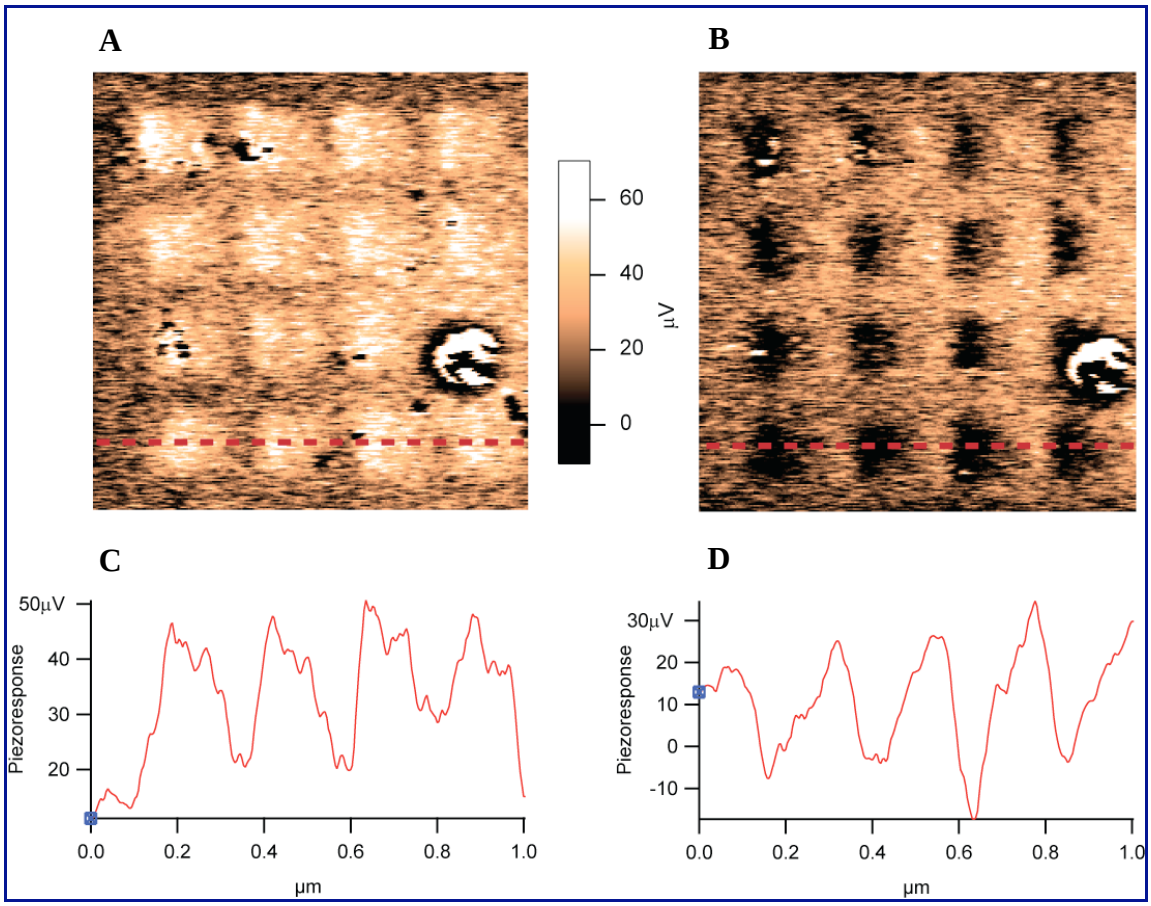


**Fig. S7.** Bistable piezoelectric response. (**A**) PFM image of a 4×4 array of square positive domains, written with $V_{tip}$ = +2 V and imaged at $V_{tip}$ = 0 V. (**B**) Same as (**A**) except that the writing voltage $V_{tip}$ = –2 V. (**C**) Linecut, shown above as a dashed line, indicating the profile of the piezoresponse for the case where $V_{tip}$ = +2 V. (**D**) Same as (**C**) except $V_{tip}$ = –2 V. The positive background piezoresponse, in the absence of poling, indicates a preferred downward orientation of the polarization of the as-grown film.

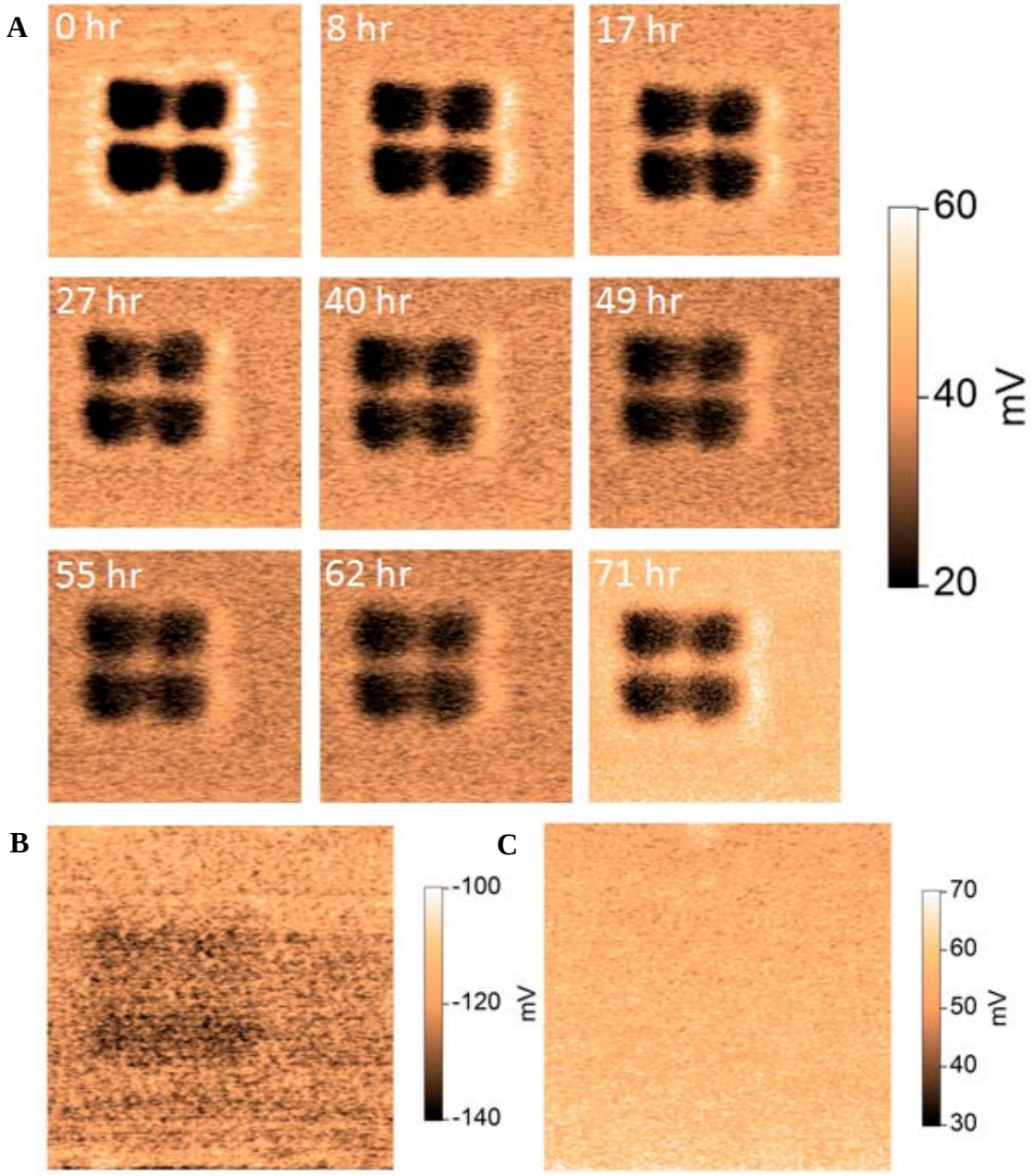


**Fig. S8.** Retention of ferroelectric domains. (**A**) Images taken at different times during the 72-hour period of a 2 μm × 2 μm area of the 6 ML thick $SrTiO_3$/Si sample that was patterned with four square domains. (**B**) PFM image obtained as the domains are being erased with $V_{tip} = -4$ V. Note the change in the color scale. (**C**) PFM image taken after erasure showing no trace of the original domain pattern.

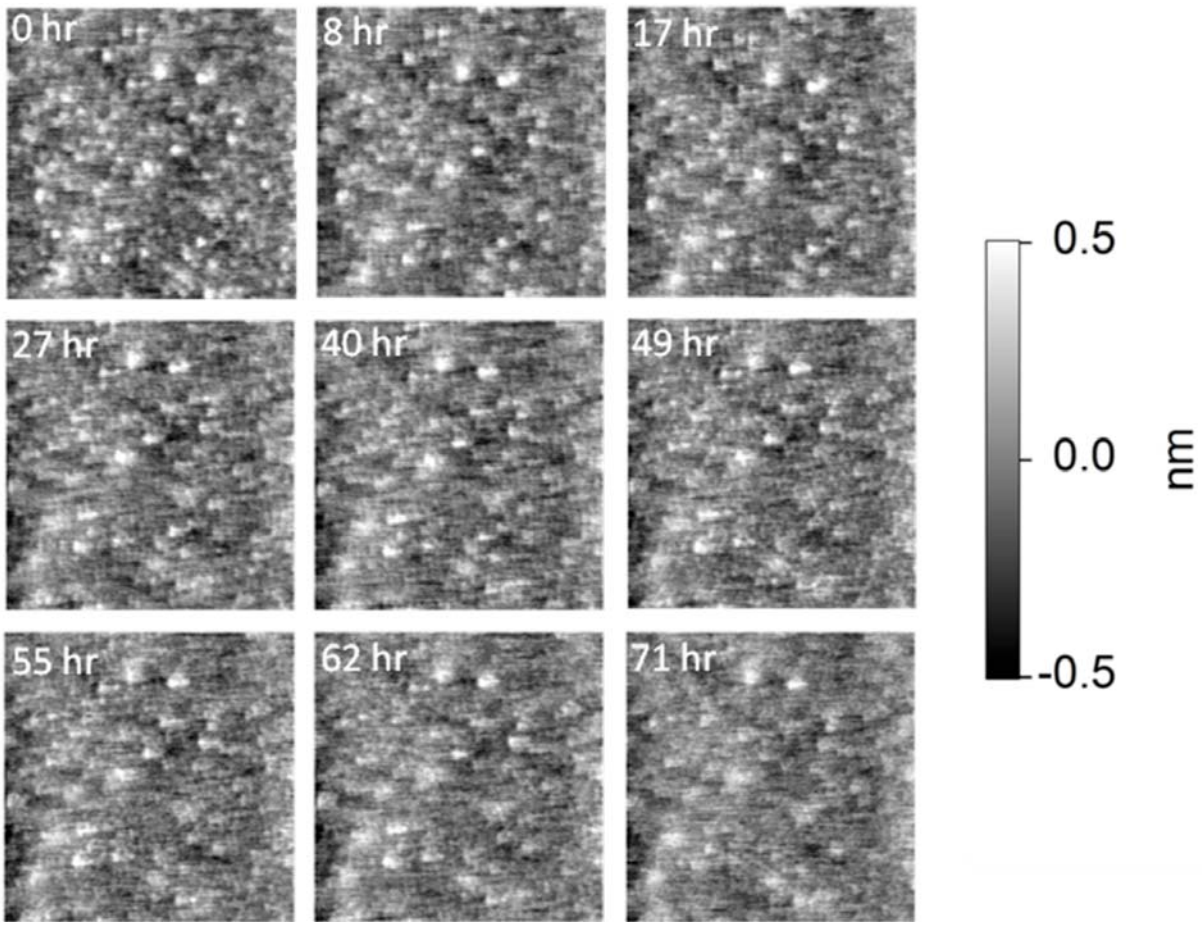


**Fig. S9.** 2 μm × 2 μm AFM topography images of the 6 ML thick $SrTiO_3$/Si sample taken simultaneously with the PFM images of Fig. S8A during a period of 72 hours. Images show a decrease in spatial resolution with time due to wearing of the tip.

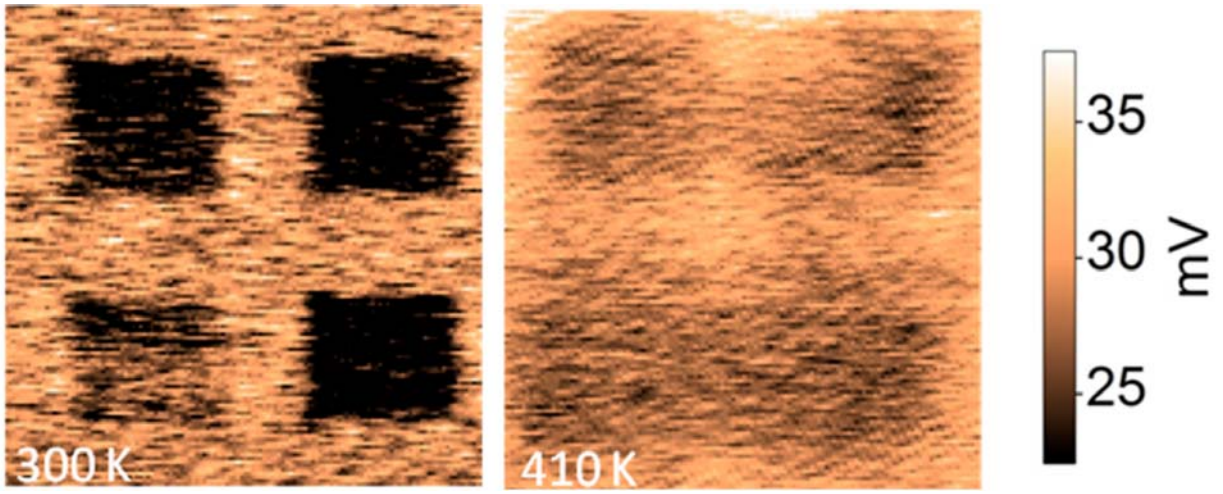


**Fig. S10.** 1 μm × 1 μm PFM image of four square domain patterns written and imaged on the 6 ML thick $SrTiO_3$/Si sample at $T$=300 K and at $T$=410 K.

**Table S1.** Phase definitions in biaxially-strained $(001)_p$ $SrTiO_3$ films.

| **Designation** | **Point Group Symmetry** | **Order Parameter (p;q)** (with respect to the pseudocubic cell) | **Equivalent Domain Variants** (with respect to the pseudocubic cell) |
|---|---|---|---|
| $\mathbf{T}^P$ | 4/*mmm* | $(0,0,0;\ 0,0,0)_p$ | |
| $\mathbf{T}^S$ | 4*mm* | $(0,0,0;\ 0,0,q_3)_p$ | $(0,0,0;0,0,-q_3)_p$ |
| $\mathbf{O}_1^S$ | *mm*2 | $(0,0,0;\ q_1,0,0)_p$ | $(0,0,0;\ -q_1,0,0)_p$, $(0,0,0;\ 0,q_1,0)_p$, $(0,0,0;\ 0,-q_1,0)_p$ |
| $\mathbf{O}_2^S$ | *mm*2 | $(0,0,0;\ q_1,q_1,0)_p$ | $(0,0,0;\ -q_1,q_1,0)_p$, $(0,0,0;\ q_1,q_1,0)_p$, $(0,0,0;\ -q_1,-q_1,0)_p$ |
| $\mathbf{T}_1^F$ | 4*mm* | $(0,0,p_3;\ 0,0,0)_p$ | $(0,0,-p_3;\ 0,0,0]_p$ |
| $\mathbf{O}_1^F$ | *mm*2 | $(p_1,0,0;\ 0,0,0)_p$ | $(-p_1,0,0;\ 0,0,0)_p$, $(0,p_1,0;\ 0,0,0)_p$, $(0,-p_1,0;\ 0,0,0)_p$ |
| $\mathbf{O}_2^F$ | *mm*2 | $(p_1,p_1,0;\ 0,0,0)_p$ | $(-p_1,p_1,0;\ 0,0,0)_p$, $(p_1,-p_1,0;\ 0,0,0)_p$, $(-p_1,-p_1,0;\ 0,0,0)_p$ |
| $\mathbf{T}_2^F$ | *4mm* | $(0,0,p_3;\ 0,0,q_3)_p$ | $(0,0,-p_3;\ 0,0,q_3)_p$, $(0,0,p_3;\ 0,0,-q_3)_p$, $(0,0,-p_3;\ 0,0,-q_3)_p$ |
| $\mathbf{O}_4^F$ | *mm*2 | $(p_1,0,0;\ 0,0,q_3)_p$ | $(-p_1,0,0;\ 0,0,q_3)_p$, $(p_1,0,0;\ 0,0,-q_3)_p$, $(-p_1,0,0;\ 0,0,-q_3)_p$, $(0,p_1,0;\ 0,0,q_3)_p$, $(0,-p_1,0;\ 0,0,q_3)_p$, $(0,p_1,0;\ 0,0,-q_3)_p$, $(0,-p_1,0;\ 0,0,-q_3)_p$ |
| $\mathbf{O}_5^F$ | *mm*2 | $(p_1,p_1,0;\ 0,0,q_3)_p$ | $(p_1,p_1,0;\ 0,0,-q_3)_p$, $(-p_1,p_1,0;\ 0,0,q_3)_p$, $(-p_1,p_1,0;\ 0,0,-q_3)_p$, $(p_1,-p_1,0;\ 0,0,q_3)_p$, $(p_1,-p_1,0;\ 0,0,-q_3)_p$, $(-p_1,-p_1,0;\ 0,0,q_3)_p$, $(-p_1,-p_1,0;\ 0,0,-q_3)_p$ |
| $\mathbf{O}_6^F$ | *mm*2 | $(p_1,p_1,0;\ q_1,q_1,0)_p$ | $(-p_1,-p_1,0;\ q_1,q_1,0)_p$, $(p_1,p_1,0;\ -q_1,-q_1,0)_p$, $(-p_1,-p_1,0;\ -q_1,-q_1,0)_p$, $(p_1,-p_1,0;\ q_1,-q_1,0)_p$, $(p_1,-p_1,0;\ -q_1,-q_1,0)_p$, $(-p_1,p_1,0;\ -q_1,q_1,0)_p$, $(-p_1,p_1,0;\ q_1,-q_1,0)_p$ |

## References


S1. Y. Wei *et al.*, *J. Vac. Sci. Technol. B* **20**, 1402-1405 (2002).

S2. V. G. Lifshits, A. A. Saranin, A. V. Zotov, *Surface Phases on Silicon: Preparation, Structures and Properties* (Wiley, Chichester, 1994), pp. 393-395.

S3. J. Lettieri, J. H. Haeni, D. G. Schlom, *J. Vac. Sci. Technol. A* **20**, 1332-1340 (2002).

S4. C. D. Theis, D. G. Schlom, *J. Vac. Sci. Technol. A* **14**, 2677-2679 (1996).

S5. R. A. McKee, F. J. Walker, M. F. Chisholm, *Phys. Rev. Lett.* **81**, 3014-3017 (1998).

S6. J. Lettieri, *Critical Issues of Complex, Epitaxial Oxide Growth and Integration with Silicon by Molecular Beam Epitaxy* (Pennsylvania State University, University Park, 2002), http://etda.libraries.psu.edu/theses/approved/WorldWideIndex/ETD-202/index.html.

S7. Z. Yu *et al*., *J. Vac. Sci. Technol. B* **18**, 2139-2145 (2000).

S8. F. S. Aguirre-Tostado *et al*., *Phys. Rev. B* **70**, 201403(R) (2004).

S9. K. Eisenbeiser *et al*., *Appl. Phys. Lett.* **76**, 1324-1326 (2000).

S10. L. H. Tisinger *et al.*, *J. Vac. Sci. Technol. B* **21**, 53-56 (2003).

S11. A. B. Shi, W. Z. Shen, H. Wu, *Appl. Phys. Lett.* **91**, 112910 (2007).

S12. Y. L. Li *et al*., *Phys. Rev. B* **73**, 184112 (2006).

S13. P. Ryan *et al*., *Appl. Phys. Lett.* **90**, 221908 (2007).

S14. H. Mori, H. Ishiwara, *Jpn. J. Appl. Phys., Part 2* **30**, 1415-1417 (1991).

S15. J. C. Woicik *et al.*, *Phys. Bev. B* **73**, 024112 (2006).

S16. J. C. Woicik *et al.*, *Phys. Rev. B* **75**, 140103(R) (2007).